

# Identifying Critical Defect Sizes From Pore Clusters in Nickel-based Superalloys Using Automated Analysis and Casting Simulation



NAOMI PIERA BELLOMO, IREM ÖZTÜRK, MICHAEL GÜNZEL, RACHEL REED, VEERARAGHAVAN SUNDAR, AMINE AMMAR, and CASPAR SCHWALBE

Porosity can form during investment casting as a result of the solidification conditions. Significant porosity can result in agglomerations (pore clusters) which are a primary crack initiation source and can result in reduced fatigue life of Nickel-based superalloys. Such clusters of porosity are today conventionally measured using 2D micrographs. An approach to accurately predict and analyze casting porosity from 2D cuts while facing in reality a 3D shape problem is currently missing. In this work, an approach that combines automation and simulation to assess the representative pore dimension, their interconnectivity and the porosity position is presented. On a LPT blade made of IN100, the porosity percentage and Feret diameter have been measured in multiple cuts and the porosity was found to be in the range of 0.88 to 5.4 pct. From the same micrographs the critical defect sizes were estimated with an automated tool to be in the range of 200 to 1800  $\mu\text{m}$ . The simulated shrinkage porosity for the same part, was predicted to be in the range of 1.67 to 2.33 pct. This study shows that the scaling factor between the pore Feret diameter and the critical pore size is equal to 2.9, in accordance to the proportionality of critical pores size clusters calculated from a 2D and 3D dataset. Finally, the simulated casting porosity was compared to that measured on cast blades in critical regions and the predictive accuracy is discussed in detail.

<https://doi.org/10.1007/s11661-023-07010-2>  
© The Author(s) 2023

## I. INTRODUCTION

NICKEL-BASED superalloys exhibit a unique combination of all the desired properties for aerospace applications, such as high mechanical strength and creep resistance at temperatures over 700 °C, good surface stability, corrosion and oxidation resistance.<sup>[1–3]</sup> Thus, jet turbine blades are typically made of nickel-based superalloys. These blades are commonly manufactured by investment casting and exhibit porosity as a routine process defect of key interest.<sup>[4–6]</sup> Porosity formation mainly occurs during metal cast solidification due to negative pressures generated during solidification

contraction.<sup>[7,8]</sup> When porosity is localized and abundant the defect is referred to as a porosity cluster in this paper. Pore clusters are a primary crack initiation source and as shown by Cervellon *et al.* can result in reduced fatigue life of Nickel-based superalloys.<sup>[9–13]</sup> Thus, to guarantee component life in the context of highly stressed aero engine components, an accurate prediction of the exact position of the defect formation is required in combination with a detailed description of the pore's features (*e.g.* pore dimension, interconnectivity of clusters and their position in a part).<sup>[14,15]</sup>

Such a prediction can be provided by the use of a porosity simulation chain that links the geometric aspect of casting porosity formation (*i.e.* shape of pore and location of formation)—and overall final quality of the cast part—with the process conditions during casting.<sup>[16–21]</sup> The accuracy of such a casting porosity defect prediction is crucial to be verified for an effective use of the simulation tool.

This study will investigate the porosity formation on a given turbine blade using thermodynamics based casting simulation and compare the accuracy of the results against metallographic cuts from the same part.

NAOMI PIERA BELLOMO, IREM ÖZTÜRK and CASPAR SCHWALBE are with the MTU Aero Engines AG, 80995 Munich, Germany. Contact e-mail: naomi.bellomo@gmail.com MICHAEL GÜNZEL is with the ESI Germany GmbH, 70565 Stuttgart, Germany. RACHEL REED and VEERARAGHAVAN SUNDAR are with the UES Inc., Robo-Met, Dayton, OH 45432. AMINE AMMAR is with the LAMPA, Arts et Metiers Institute of Technology, 49035 Angers, France.

Manuscript submitted August 31, 2022; accepted February 9, 2023.  
Article published online March 23, 2023

Next, the study will investigate the porosity size, shape and associated critical defect size seen in turbine components in 3D and compare this to 2D images from these components.

Today, the analysis of porosity in industrial investment casting is commonly done manually.<sup>[22–24]</sup> However, this method is not sustainable, because it requires high investment in time and cost for manpower and material. The most critical disadvantage comes from the fact that such manual analysis lacks reproducibility.<sup>[25]</sup> The manual checks are done on two dimensional (2D) images of porosity clusters that are three dimensional. Therefore, the plausibility of defect size measurements acquired from 2D images needs to be investigated. This study will investigate a cost competitive, accurate and reproducible approach to detect critical pore clusters sizes on 2D images with the use of image detection and analysis.

## II. METHODS

This study investigates porosity in a given low pressure turbine blade cluster (LTP) made of the alloy IN100 with a nominal chemical composition outlined in Table I. The LPT blades were cast under vacuum. Usually these parts are subsequently hot isostatically pressed to reduce the critical defect sizes and reduce porosity. However, for the purpose of this work the blades were analyzed immediately after casting and without further processing.

Firstly, four cast blades from the cluster were cut and analyzed using light microscopy. Secondly, the micrographs obtained from the different cuts were analyzed and then processed with an automated script written in Python™(*Python Software Foundation*) to characterize the observed porosity. The Python script was validated by comparing the accuracy of the 2D metallographic cuts with a serial sectioning technique conducted by Robo-Met.3D ®(*UES, Inc. OH*) that delivered 3D rendered information on porosity sizes. Thirdly, the casting process parameters were used to setup a casting simulation of the blade cluster array using the commercial software ProCAST.\* The casting simulation was then analyzed in terms of total shrinkage porosity and compared to the metallographic cuts of the same geometry to validate the accuracy of the simulation.

### A. ProCAST Model

The 3D model of the investment casting simulation aims to reproduce the exact experimental conditions of the selected low pressure turbine blade, cast under the process conditions defined by the casting house. Thus, the model setup goes through the following main steps:

**Table I. Nominal Chemical Composition of the Nickel Based Superalloy IN100 (wt Pct)**

Co	V	Mo	Cr	B	C	Ti	Al	Zr
14.9	1.02	3.1	10.1	0.01	0.18	4.57	5.53	0.05

Adapted from Ref. [26]

- preparation of the CAD model, including the blade geometry and gating system
- creation of the ceramic shell and insulation system
- setup of the process condition

The mold consists of 12 blades organized in two rows and oriented as described in Figure 8. In order to reduce the computational time of the simulation, the CAD model was simplified using the symmetry plane between the blades 4 to 6 and 10 to 12 as well as between the blades 1 to 3 and 7 to 9. Thus, only the blades 4 to 6 and 10 to 12 have been included in the CAD model and simulated as they mirror the other half.

The shell was created with a constant thickness of 9 mm. The insulation system consists of an inner layer between the two rows and three outer layers of 12 mm each. The materials properties of the alloy were calculated with Computherm, using the chemical composition outlined in Table I. For the calculation with Computherm, the chemical elements with a content lower than 1 wt pct (B, C, Zr) were not included. The material properties (*e.g.* thermal conductivity, density *etc.*) of the ceramic and insulating material were taken from the ProCAST material database.<sup>[16,27]</sup>

The overall process was modeled consisting of the following three main steps:

- *transport* of the mold from the pre-heating chamber to the casting furnace
- *filling* of the mold under vacuum with the alloy
- *solidification* of the alloy.

### B. Metallographic Analysis

After the manufacturing process was completed, blades number 3, 6, 7, and 10—indicated by shading in Figure 8—were cut up for the subsequent metallographic porosity analysis. For the investigation, the optical microscope *Axio Imager.M2m* (*Carl Zeiss AB, SE*) was used. Each blade was cut in nine different positions as shown in Figure 5 (left). Samples were cold mounted in EpoFix resin and EpoFix hardener and surfaces were polished with silica paper up to 1  $\mu$ m finish. For each cut, micrographs with an overall magnification of  $\times 2.5$  and  $\times 5$  were taken. Then, images were analyzed with the post processing software IMAGIC IMS ®(*Imagic Bildverarbeitung AG, CH*) to measure the pores—on all micrographs for both magnifications—and the maximum Feret diameter<sup>[28]</sup> only on micrographs taken at  $\times 2.5$  magnification.

\*ProCAST is a Finite Element casting simulation software edited by ESI Group.

### C. 2D Automated Pore Detection

The influence of a pore on the mechanical properties depends on several aspects such as their shape, position and size. With today's imaging limitations it is not possible to routinely acquire a 3D rendering of all pores contained in each commercial part. In light of this it is commonly accepted to consider the largest defect as the key parameter that governs the parts fatigue resistance.<sup>[29]</sup> Furthermore, if the distance between two pores is less than a critical distance, it is expected that the crack nuclei corresponding to the pores will unite after a few load cycles.<sup>[30]</sup> Such pores are thus referred to as a pore cluster and this usually represents the life-limiting crack initiation site.

The industry standard manual examination of micrographs is usually time demanding and crucially the results are difficult to reproduce. Therefore, a tool for an automated porosity defect size assessment was developed.<sup>[31]</sup> The developed algorithm can be divided into three principal parts: Structural analysis, Defect size estimation and Validation (see Figure 1).

The structural analysis takes raw micrographs as an input. Two types of images are analyzed:

- Overview images allowing to observe a larger area, evaluate porosity percentage and identify pore clusters. The resolution of these images is not sufficient to perform a quantitative analysis of pore sizes.

- Pore cluster images representing a 1 mm<sup>2</sup> area containing pore clusters. These images are used to analyze and extract pore properties.

After identifying the image type, the algorithm applies a classic preprocessing procedure to facilitate the subsequent image analysis (*e.g.* Erosion, Dilation, Opening, Closing). Non-local noise reduction algorithms are then applied before using the Otsu thresholding method<sup>[32]</sup> to binarize the image. The findContours function from opencv library<sup>[31]</sup> showed the best performance in detecting pore contours on binarized images. The output of this part is a dataframe containing the calculated results (*i.e.* pores centroids positions, areas, perimeters). The defects size estimation part takes the information from the previous step and, first of all, identifies the different clusters based on the distance between the observed pores. Different algorithms have been implemented: Hough transformation,<sup>[33]</sup> K-means<sup>[34]</sup> and PCA analysis<sup>[35]</sup> and critical distance method.<sup>[36]</sup> Subsequently, two methods were compared to estimate the equivalent defect size of a cluster: bounding rectangle<sup>[36]</sup> and pore area model.<sup>[29,30,37]</sup> The output of this part is represented by the biggest cluster and the corresponding equivalent defect size.

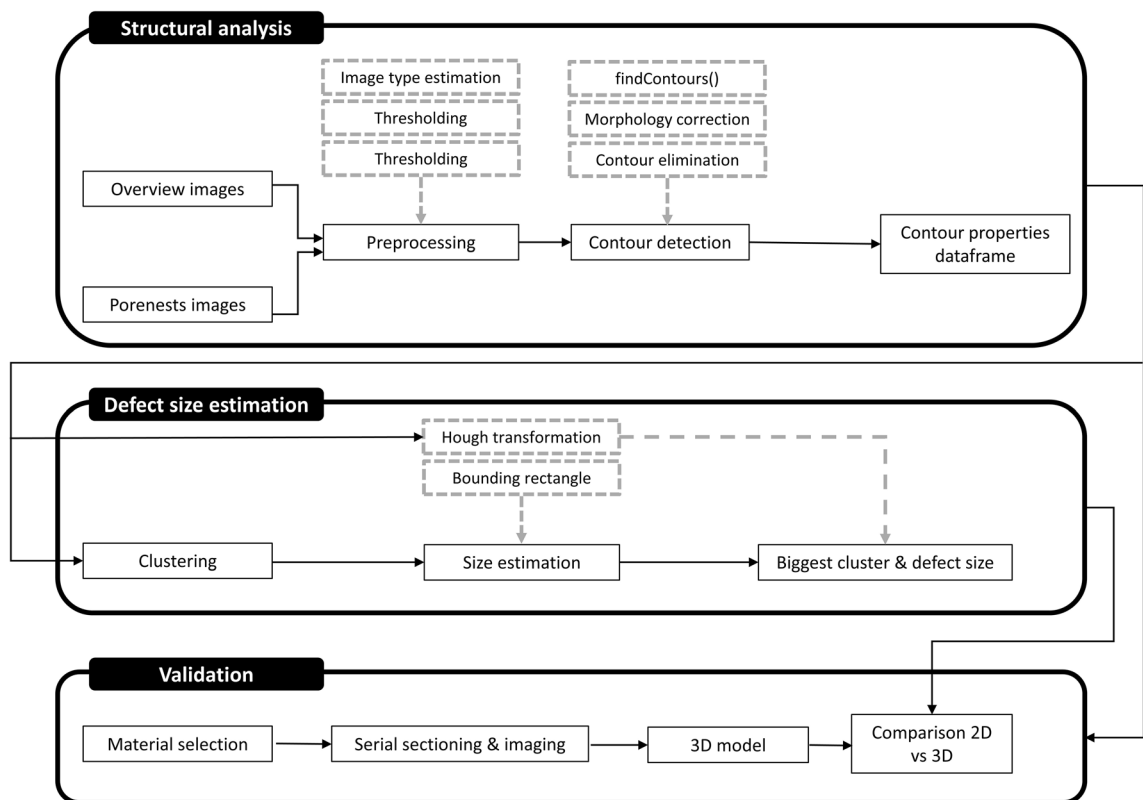


Fig. 1—Workflow of the automated pore analysis and defect size estimation model.

The results from the previous steps were validated by comparing them to a manual estimation on 2D images and 3D renderings. The 3D renderings were obtained using the Robo-Met automated serial sectioning method, that reconstructs the 3D shape of pores and thereby allows a better understanding of the pore interconnectivity.<sup>[38]</sup> The critical distance criterion showed the most similar results to 2D manual estimation (10 pct error) and 55 seconds per image for the analysis. The pore area model yields substantially lower values than manual estimates, which makes it unsuitable. The comparison between bounding rectangle results and validation *via* 3D renderings proved that this method performs the most valid and plausible defect size estimation, with a 85 pct precision.<sup>[31]</sup>

#### D. 3D Porosity Evaluation

Casting pores can present itself as highly irregular, yet interconnected structures (see Figure 2 right). The true interconnectivity of such a pore structure can be hidden when performing a 2D metallographic cut [compare the white dashed region in Figure 2 left (2D) to the right (3D)]. Consequently a 3D quantitative analysis is required to validate the 2D results.<sup>[39]</sup> The verification of the 2D automated tool described in Section III was performed using the fully automated materials characterization system Robo-Met 3D.<sup>[38]</sup> This technique is able to recreate 3D microstructural data from serial sectioning. For the purpose of the verification, three different cuts consisting again of the alloy IN100 were selected and sent to Robo-Met for serial sectioning and 3D rendering (see Öztürk<sup>[31]</sup> for further details of the study parameters).

To demonstrate the influence of a local 2D cut, the variation of porosity size and frequency was plotted. Figure 3 shows the data extracted from sectioning a part in 100 equal  $x$ - $y$  planes which only vary by their  $z$ -height and then plotting every 10th sections porosity frequency versus the maximum Feret diameter in grey. The red line in Figure 3 plots the average values across all eleven sections. Larger defects have a significant impact on fatigue life and to exhibit these infrequent yet critically large pores the  $y$ -axis was plotted logarithmically. Figure 3 offers the hypothesis that finding the largest defect in 2D sections is purely based on probability.

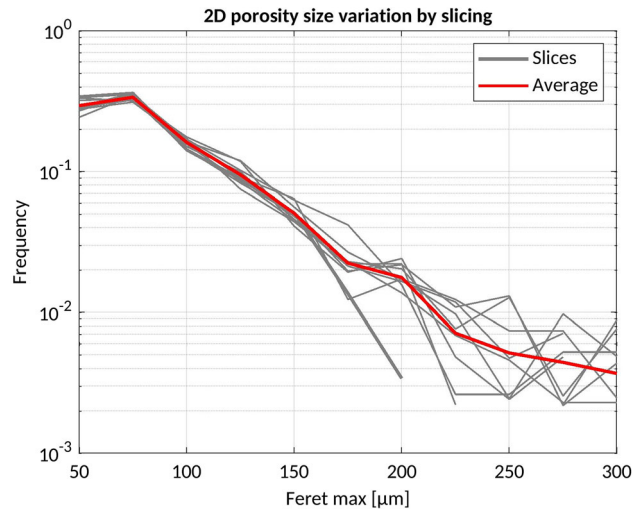


Fig. 3—Frequency of occurrence of the pores' Feret diameter over eleven 2D slices. The black curves show the dataset for each of the evaluated slices. The red curve plots the average values across all eleven sections.

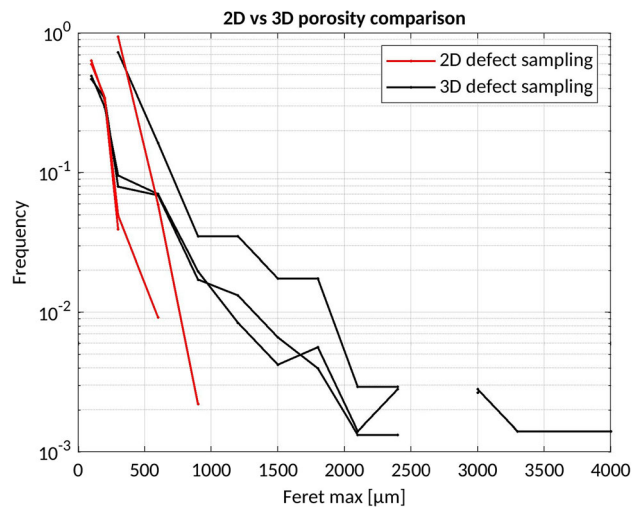


Fig. 4—Comparison of the porosity frequency of the three different samples plotted over the maximum Feret diameter. The black curves show the dataset evaluated using 3D rendering of interconnected pores and the red curves show the same dataset using selected 2D average slices from the three samples only.

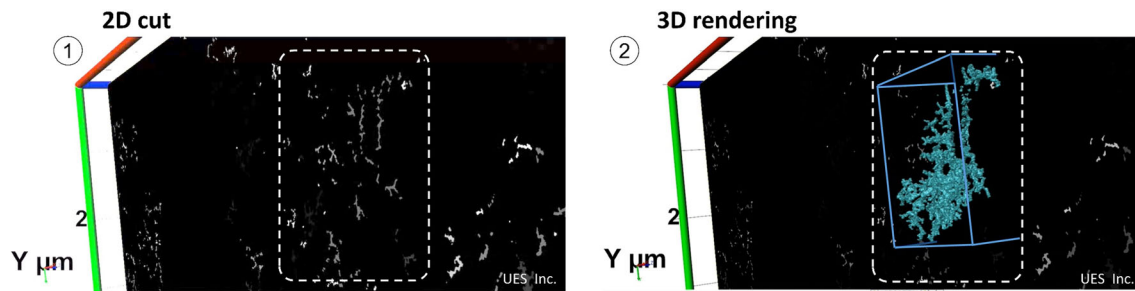


Fig. 2—Comparison of a pore representation between (1) a 2D cut and (2) 3D rendering, courtesy of Robo-Met.



However, when plotting the 2D average porosity frequencies versus their maximum Feret diameters for the three sections and comparing them to the true 3D values in Figure 4 it becomes clear that the likelihood of capturing the maximum Feret diameter in the 2D imaging plane is extremely unlikely. The 3D verification thus revealed that porosity measures such as maximum Feret cannot capture critical porosity accurately and that a critical defect parameter (*i.e.* bounding rectangle) as outlined by Öztürk<sup>[31]</sup> is essential to capture conservatism in an industry context. In the following section the critical defect size as estimated by Öztürk<sup>[31]</sup> is used to put into context the porosity found in the sections of the cast LPT blades.

### III. RESULTS

#### A. Metallographic Porosity Detection

The cast IN100 blades were cut up into nine different slices labeled A–I (see Figure 5 left). The optical microscopy images at  $\times 2.5$  magnification are shown for cuts A–E and G–I of blade 3 in Figure 5 right. The cut F (due to its thin section) was imaged at  $\times 10$  magnification. Looking at the cut planes in Figure 5 casting porosity (in this case shrinkage porosity) can be observed as black irregular structures on all cuts. In addition to porosity, smaller grey spots with a periodic arrangement are visible. These grey structures are eutectic phases, located in the interdendritic regions. In

detail, the porosity in slices A is homogeneously distributed throughout the cut and the pores have a comparable size and non-spherical shape. The porosity in slices B–E exhibit individual pores that exceed the largest feature seen in cut A. The last cut of the turbine airfoil, slice F seems to exhibit the lowest amount of porosity overall. The cuts G–I, which are taken across the blade root, appear to exhibit similar porosity levels to the B–E airfoil cuts. Roskosz<sup>[40]</sup> detected a comparable level of porosity in non HIP-ed IN713C with maximum porosity levels located at the relative airfoil height corresponding to cuts B–E in Figure 5. However, the root cuts seem to also show the highest amount of eutectic phases.

The porosity percentage of the cuts was measured using the IMAGIC IMS software and the values for blade 3 are presented in Table II. Measured porosity was found to be highest in cut G (blade root) and lowest in cut F (airfoil shroud). Further, porosity is found to be lower in the central area of the airfoil (cuts C and D).

#### B. 2D Porosity Evaluation

Using the bounding rectangle approach in the automated porosity cluster calculation tool described in Section II–B all optical micrographs were analyzed at  $\times 2.5$  and  $\times 5$  magnification. Four different types of results were obtained using this approach and a representative output using images for each of the four types

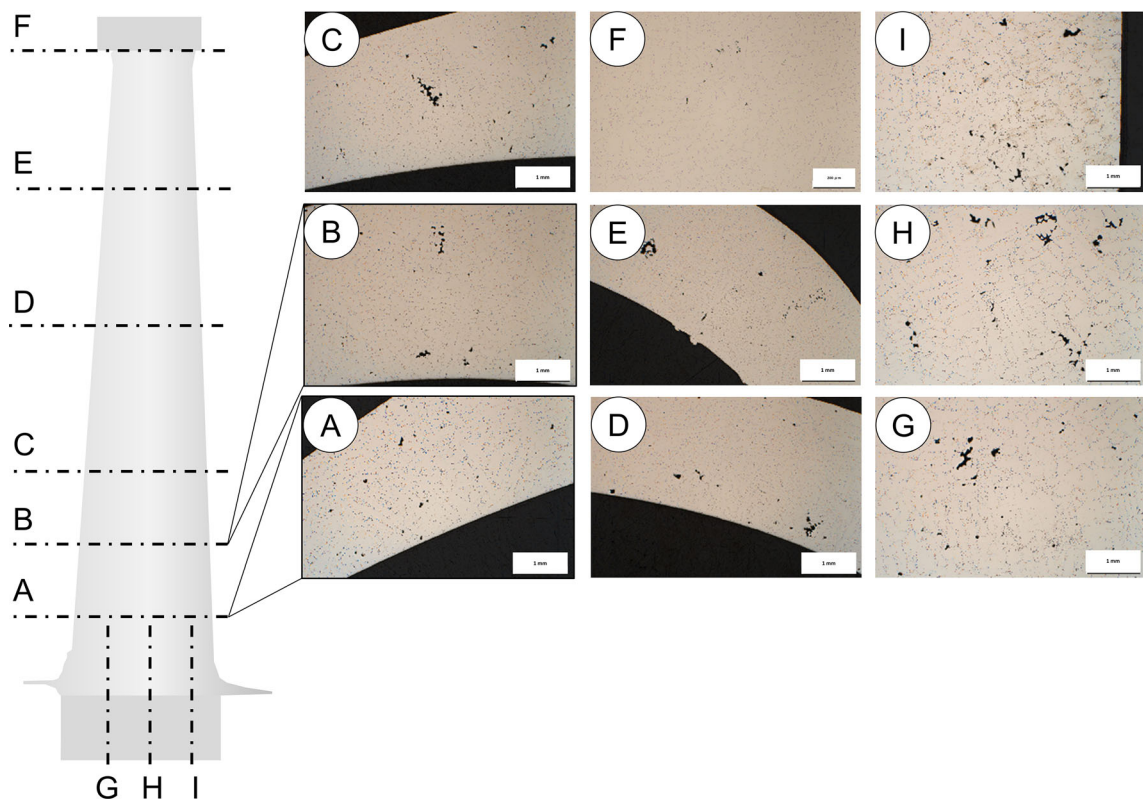


Fig. 5—(left) Sketch of the nine cut locations performed on each cast blade. (right) Pore detection with optical microscope on blade 3 on cuts A to I with a magnification of  $\times 2.5$  except for slice F that has an optical magnification of  $\times 10$ .

is shown in Fig. 6 (images presented are from blades 6 and 7). In subfigure 1 of Figure 6 the first type of result is shown. Here the bounding rectangle (indicated by a green box) includes not only casting porosity but also eutectic phases. The grey value of the eutectic phases were above the defined threshold value for the image binarisation and are thus falsely classified as porosity (see Section II-C). The biggest defect identified by the tool (indicated by a black arrow) is thus significantly larger than the pore cluster it contains. This first type of result is a false positive reading and the calculated critical defect sizes of such readings were declared non-valid and not used for further analysis.

The second type of result is shown in subfigure 2. Here, the thresholding again mislabelled eutectic phases as porosity in some instances. However, the largest

defect cluster (indicated by a black arrow) was correctly found and the critical defect size estimated for type 2 images was used in the further analysis.

Subfigure 3 shows the third type of result. The largest pore cluster was correctly found (indicated by a black arrow) and no interference from the eutectic phase is visible. Some minor porosity was however missed (indicated by a white arrow). Since the missed porosity did not impact the result of the critical defect size estimation, the values calculated for type three were deemed valid and used in the further analysis.

The last type of result visible in the dataset concerns the difference in the field of view and resolution between images of  $\times 2.5$  and  $\times 5$  magnification. For comparison an image of  $\times 2.5$  magnification is shown in subfigure 4 and one with  $\times 5$  magnification in subfigure 5 of the same blade 7. The overall largest defect is indicated by a white triangle, this defect is outside of the field of view in subfigure 5 and thus is only visible in subfigure 4. Furthermore, defects on the edge of the field of view, like that indicated by a black triangle are truncated by the edge of the image and appear smaller in subfigure 5 than they are (compare to subfigure 4).

To compare the measured porosity to that simulated a suitable magnification needs to be selected. The calculated critical defect sizes for the  $\times 2.5$  (black symbols) and  $\times 5$  magnifications (red symbols) are plotted in Figure 7. Comparing the population from  $\times 2.5$  and  $\times 5$

**Table II. Porosity Percentage Measured with IMS on the Micrographs in Fig. 5**

A	B	C	D	E	F	G	H	I
0.88	1.43	3.64	2.03	2.82	0.05	5.43	3.64	2.25

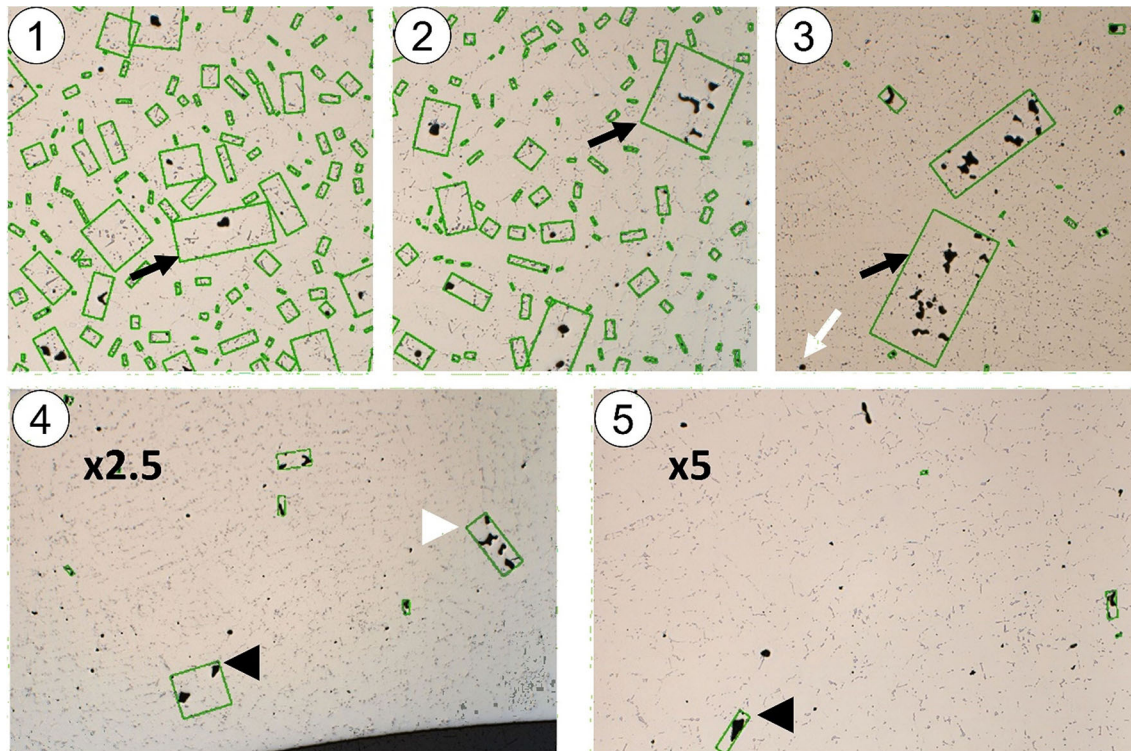


Fig. 6—Calculated pore clusters on optical micrographs of blade 6 and 7: (1) False eutectic indication on blade 6—magnification  $\times 2.5$ —slice I; (2) False eutectic indication but largest cluster identified, blade 6—magnification  $\times 2.5$ —slice H; (3) No eutectic indications and correctly labeled largest cluster, blade 6—magnification  $\times 2.5$ —slice C; (4) Field of view comparison, blade 7—magnification  $\times 2.5$ —slice A; (5) Field of view comparison, blade 7—magnification  $\times 5$ —slice A. The black arrows point at the largest defects, the white arrows points at the defect that are not recognized. The black triangle point at the same defect location in subfigure 5 and 6 for comparison and the white triangle points at the largest defect in subfigure 4 that is outside the field of view in subfigure 5.

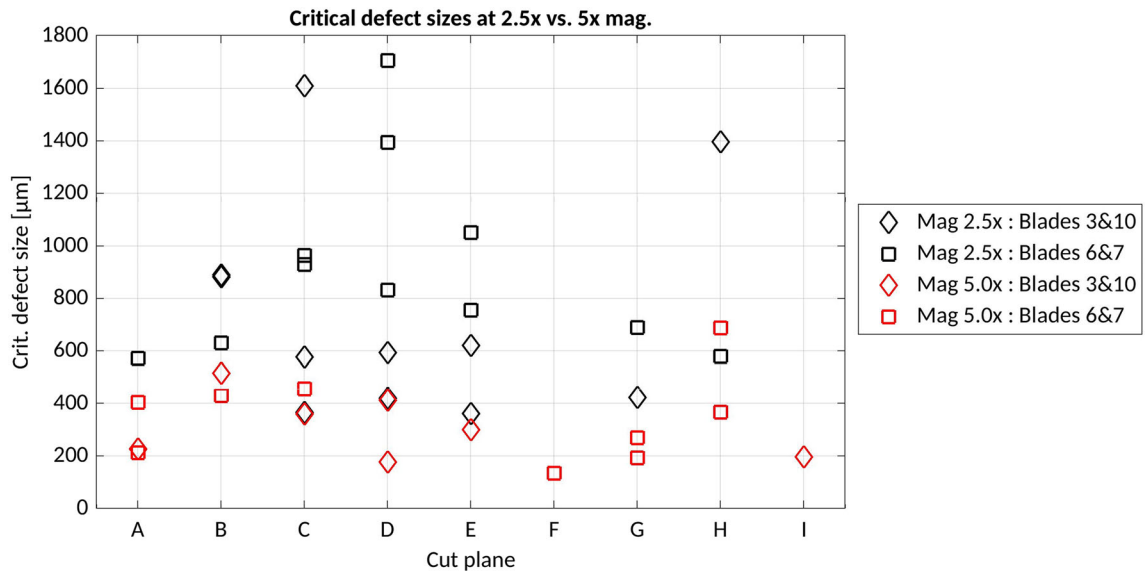


Fig. 7—Critical defect size measured by the 2D automated tool on the micrographs for the cutting planes from A to I with an optical magnification of  $\times 2.5$  (black markers) and  $\times 5$  (red markers). Values obtained from blade mirror pairs 3 and 10 are plotted with diamond and blades 6 and 7 with square markers.

it is evident that the lower magnification resulted in a higher success rate (56 pct of all images were of type 2 and 3 vs. 36 pct for the  $\times 5$  magnification) and thus contains a larger dataset. The thresholding of the image seems to thus work better in terms of removing the false detection of eutectic phases on images with a wider field of view (less type 1 errors). Furthermore, the lower magnification contains larger critical defect sizes (largest defect at  $\times 2.5$  is  $1705 \mu\text{m}$  vs.  $514 \mu\text{m}$  for  $\times 5$ ). This seems to be due to the larger magnification missing most of the critical defects in its narrower field of view (less type 4 errors).

Lastly, the influence of higher resolution on the accuracy of the defect size measurement was checked. The largest critical defects that were successfully detected by both magnifications (blade 10 cut C and D as well as blade 6 cut F) were directly compared. For example the critical defect size in blade 10 cut C was estimated as  $366.8 \mu\text{m}$  at  $\times 2.5$  and  $360.9 \mu\text{m}$  at  $\times 5$  magnification. Overall the higher resolution resulted in a reduction of the critical defect size by 0.75 pct. Thus, the increased resolution comes only with a marginal improvement of accuracy in terms of individual defects but a large debit in accuracy in terms of detection. Therefore, only images with a magnification of  $\times 2.5$  were used for the comparison of overall porosity in a cast turbine blade vs. the casting simulation.

### C. Porosity Simulation with ProCAST

The casting simulation set-up described in Section II–A was used to estimate the distribution of total shrinkage porosity percentage throughout the solidified blade cluster after the casting process. The shrinkage porosity is predicted accordingly to the model implemented in ProCAST, which is based on the comparison of the local solid fraction (FS) with three parameters

corresponding to crucial steps of the solidification process.<sup>[16,41]</sup> Representative output of the simulated shrinkage porosity is presented in Figure 8.

The left side of Figure 8 shows the blade cluster array, labeling all 12 blades. On the right side of Figure 8 the ProCAST output for blades 3 and 10 of predicted shrinkage porosity is presented for each of the nine cuts (A–I) previously performed on the cast blades (compare to labels Figure 5, left). The simulation results indicate a shrinkage porosity in the range of 1.67 to 2.33 pct is to be expected with the defined casting parameters. Examining the porosity trends it can be seen that the porosity profiles for slices A to D are similar to each other and exhibit a higher porosity in the inner section of the airfoil profile. These findings align with Yang *et al.*<sup>[42]</sup> who observed these trends simulating top filling conditions also, but for titanium aluminide. Further, slice F is estimated to have the lowest amount of porosity, whereas porosity in the blade roots is expected to be higher. The innermost areas of the blade root sections are predicted to have the highest porosity in the lateral regions (up to 2.33 pct shrinkage porosity expected). The overall trends for the porosity match those observed on the cast blade in Figure 5, right (see Section III–A).

## IV. DISCUSSION

To conclude on the accuracy of the simulated porosity estimated with ProCAST this study seeks to compare it against the porosity found in the nine different cut locations of the cast blades. The shrinkage porosity simulated with ProCAST is a location specific percentage porosity estimated as described by Torroba *et al.*<sup>[16]</sup>. To compare this to the porosity found in cast blades of the same geometry and processing conditions firstly the different techniques to measure and estimate porosity



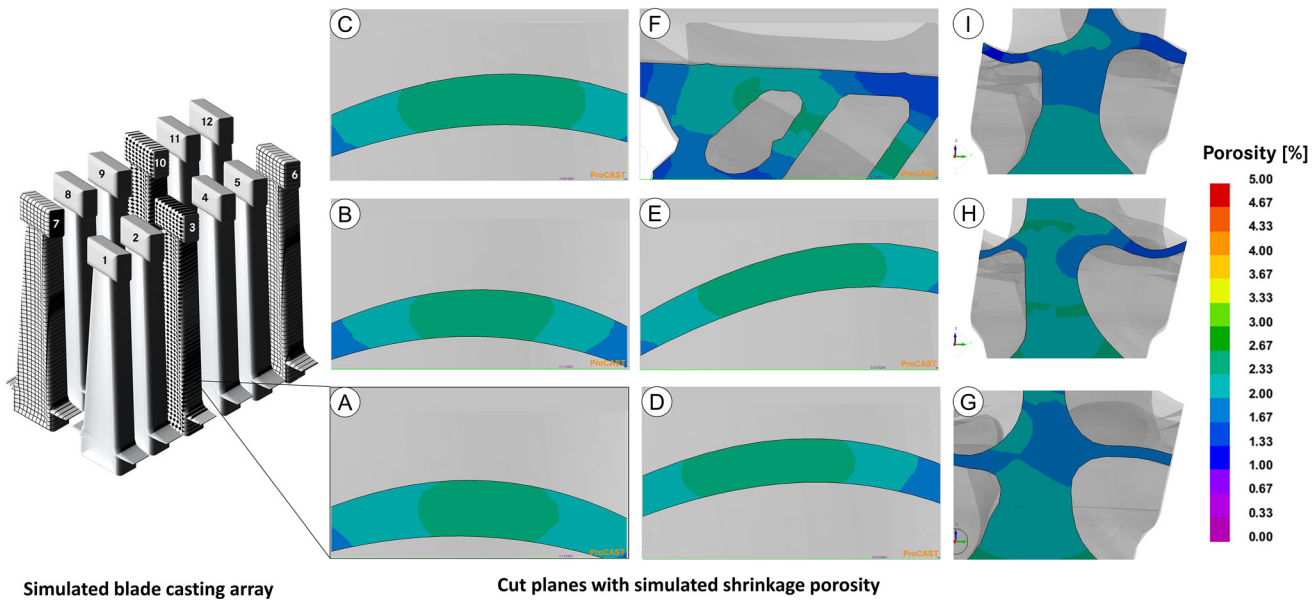


Fig. 8—(left) Sketch of the casting blade cluster array for the 12 blades. Blades selected for examination are shaded in their corresponding symmetry pairs (blades 6 and 7 as well as 3 and 10). (right) Simulated total shrinkage porosity [pct] by ProCAST for blade 10 and 3 shown for each of the nine cut locations A-I selected for the cast blades (see sketch in Fig. 5 left).

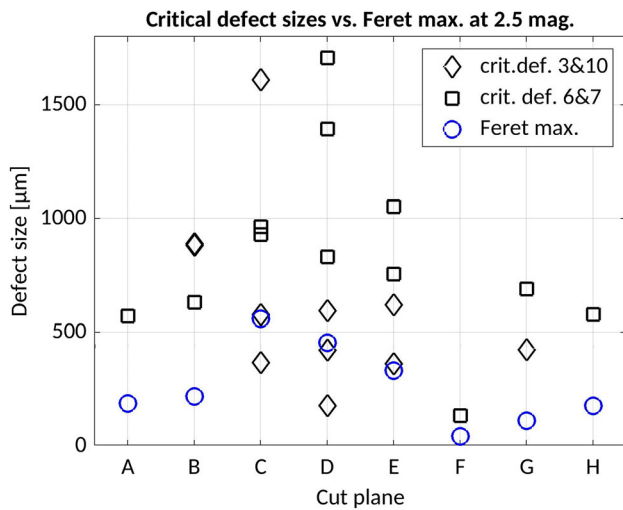


Fig. 9—Defect sizes in  $\mu\text{m}$  for cut planes A-H comparing critical defect sizes (from the 2D automated tool plotted as black diamonds for blades 3 and 10, and black squares for blades 6 and 7) against the maximum Feret (measured by IMS for the maximum porosity image across all blades for each cut location, plotted as blue circles). For both measurements optical micrographs with  $\times 2.5$  magnification were used.

need to be discussed and secondly the accuracy of the simulation set-up need to be discussed.

#### A. Determining Accurate Porosity Information from 2D Metallographic Cuts

Three different methods can be used to analyze the 2D optical microscopy cuts, maximum Feret diameter and area porosity percentage estimated by IMS as well as critical defect size computed by the automated tool.

Figure 9 compares the the maximum Feret diameter against the critical defect. The critical defect size was calculated by the 2D Python script on all the micrographs of blades 3 and 10 (black diamond markers) and 6 and 7 (black square markers) with an optical magnification of  $\times 2.5$ . The maximum Feret diameter was only calculated for the images with the highest critical defect sizes for each blade cut. From cut A to H the maximum values were found in the following blades 7, 10, 3, 7, 7, 6, 6, and 6. For all cuts the critical defect size for these blades is significantly larger than the maximum Feret diameter (2.9 times larger and  $R^2$  equals to 0.9). This factor aligns well with the factor observed when comparing the 2D and 3D dataset in Section II-D. Thus, the critical defect size method seems to be a suitable measure to estimate the largest pores in a given 2D cut of a cast blade.

#### B. Determining the Accuracy of the Automated Porosity Evaluation

Applicability of the critical defect parameter can be further strengthened through the analysis displayed in Figure 10. If critical defect size is an adequate measure to assess the 2D porosity, then a proportional relationship between it and the measured maximum porosity would be expected. This assumption is based on the findings that higher percentage of porosity translates into larger critical defect sizes.<sup>[43]</sup> Figure 10 plots the maximum critical defect sizes for each cut over the measured maximum porosity in the same cut (red squares). Black circles represent the maximum Feret diameter values plotted over the maximum porosity. Dashed lined and overlaid  $R^2$  values display the result of a linear regression analysis of each dataset in corresponding colors. Looking at the obtained fit functions it



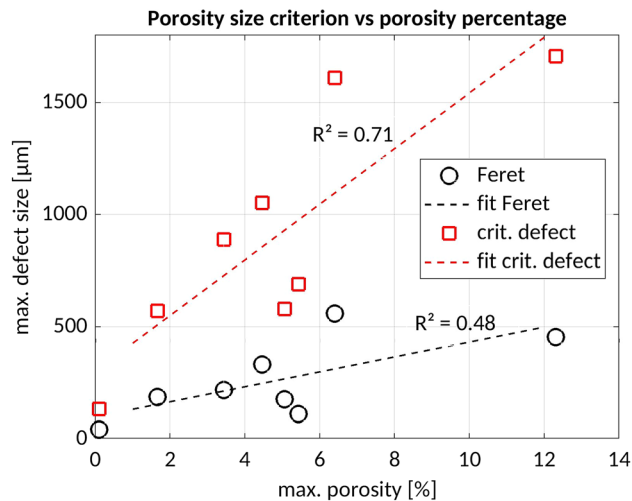


Fig. 10—Relationship between the maximum porosity percentage measured on a cut by IMS plotted against the critical defect size estimated by the automated tool (red squares) or the maximum Feret measured by IMS (black circles). The correlation fit between both values is plotted as a dashed line in corresponding color with  $R^2$  given for the fit.

can be concluded that the critical defect size estimated by the automated Python tool is indeed proportional to the maximum porosity percentage. Based on this finding it is likely that the porosity percentage calculated by the IMS tool in each cut of the blades are proportional to the likelihood of critical defects present in these cuts. Therefore, in a next step the porosity obtained by IMS in all cuts and all blades of the  $\times 5$  magnification (the standard magnification for porosity imaging) were compared to the simulated values obtained by ProCAST (see Figure 11).

### C. Determining the Accuracy of the Simulated Porosity

In Figure 11, the porosity percentage measured by the IMS tool (marked with black crosses for the mean values and black plusses for the median) is compared against the equivalent values, for all the cut planes predicted by ProCAST (red circles markers). The grey bars represent the variation between the minimum and maximum porosity measured. The scatter bands marked by the grey lines thus show the variation in the dataset of each cut aligns with the indicators for a normal distribution. Thus, cuts D, F, G and H have the highest variations while the remaining cuts display lower data deviation in the porosity dataset. The comparison between mean and median values gives an indication if the data could be normal Gaussian distributed (cuts A, E, F, H, I), the data could contain a tail (cuts B, C, G) or might be significantly affected by a few larger pore indications and exhibit a significant tail (cut D). The ProCAST dataset however assumes a normal porosity distribution and cannot match findings like that displayed in cut D. Whilst ProCAST seems to be able to predict the expected maximum porosity in cuts B, C, H within the data variation band or even close to the average values (cuts E, G, I) a deviation is visible for cuts A, F (and D as discussed above). For these cuts the

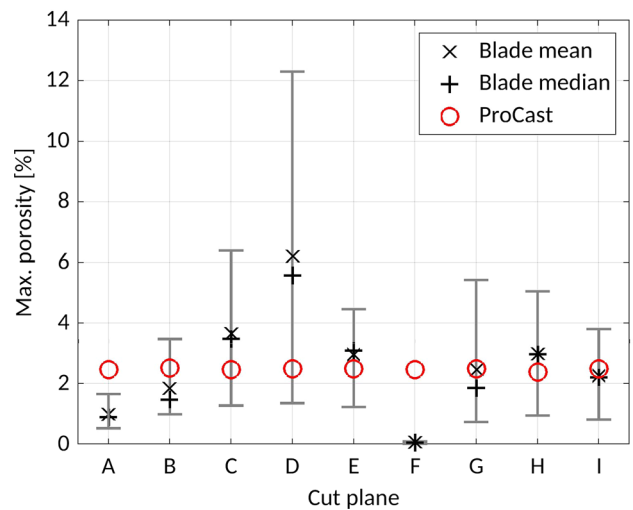


Fig. 11—Comparison of porosity percentages measured by the IMS tool (black and grey data) against the values predicted by ProCAST (red circles) for cut planes A–I. The grey lines show the variation between the minimum and maximum porosity measured, the black x represent the mean and the black + the median porosity percentage of the dataset for each cut location.

dataset indicates a normal distribution but the simulation was unable to correctly reflect the experimental observation in these cuts. Having directly applied the processing parameters of the cast blades, the principal source for the deviation in the ProCAST simulation is expected to originate from the description of the ceramic shell and the alloy properties. As outlined in Section II–A, both the shell and the insulation have been modeled assigning to them a constant thickness. However, a lower thickness of the ceramic should be expected in the rounded profiles of the mold, especially on the blades profile.<sup>[44]</sup> Furthermore, the ceramic shell has a so called sandwich structure, resulting in a certain percentage of air trapped inside the shell. This, combined with the non constant thickness of the shell, has a significant influence on the actual thermal conductivity of the ceramic, thereby directly influencing the heat exchange between the alloy and the mold<sup>[16]</sup> and thus having an impact on the degree of shrinkage porosity in the cut locations A, D and F. Consequently, an experimental characterization of both the ceramic and alloy is fundamental for an accurate modeling of the heat transfer coefficient between the alloy and the mold as well as between the mold and the insulation.<sup>[16,45]</sup>

The alloy chemistry influences the porosity simulation through its thermodynamic property description *via* Computherm (see Section II). To save computation time the three minor element additions of lower than 1 wt pct in Table I were not considered when computing the thermodynamic alloy properties. However, even such minor element additions can have a significant impact on the solidus and liquidus temperatures. Zhou *et al.* for example found that an increase of Zr from 0 to 5000 ppm can lower the solidus temperature by 20 K and the liquidus of 9 K. This change of values directly impacted the simulated porosity and resulted in a 0.5 pct increase of micropores.<sup>[46]</sup>

## V. CONCLUSIONS

The two principal questions this study tries to investigate in the context of industrial investment casting series production are how to accurately analyze or predict casting porosity from 2D cuts when faced with a 3D shape problem and can casting simulation accurately predict shrinkage porosity in a blade cluster array. The main conclusions of this work are the following:

- The critical defect size method used by the referenced 2D automated tool is a suitable (time and cost efficient) and conservative measure to identify and measure the largest pore cluster in a 2D micrograph. The average scaling factor of 2.9 matches the 3D size factor observed *via* serial sectioning.
- Maximum porosity percentage measured in a 2D micrograph display significant correlation to the critical defect size measured by the developed automated tool. Both parameters were thus used to link the simulated shrinkage porosity percentage to the likelihood that a pore cluster with a critical defect size is contained in the same micrograph.
- Casting simulation was able to accurately predict casting porosity in 6/9 regions of the blade cluster. Future research seeks to clarify how the level of predictive accuracy can be significantly enhanced.

## ACKNOWLEDGMENTS

The Bavarian State Ministry for Economic Affairs, Regional Development and Energy (StMWi) within the framework of the aeronautical research program BayLu25-II and MTU Aero Engines are acknowledged for financial support. M. Futoma, R. Sowa, M. Panella (MTU Aero Engines) are acknowledged for the valuable discussions on this work. C. Schwaminger and C. Bader (MTU Aero Engines) are acknowledged for providing the metallographic analysis. T. Göhler (MTU Aero Engines), J. Artozoul and I. Tiba (LAMPA, Arts et Metiers Institute of Technology) are acknowledged for their valuable discussions and input.

## CONFLICT OF INTEREST

On behalf of all authors, the corresponding author states that there is no conflict of interest.

## OPEN ACCESS

This article is licensed under a Creative Commons Attribution 4.0 International License, which permits use, sharing, adaptation, distribution and reproduction in any medium or format, as long as you give

appropriate credit to the original author(s) and the source, provide a link to the Creative Commons licence, and indicate if changes were made. The images or other third party material in this article are included in the article's Creative Commons licence, unless indicated otherwise in a credit line to the material. If material is not included in the article's Creative Commons licence and your intended use is not permitted by statutory regulation or exceeds the permitted use, you will need to obtain permission directly from the copyright holder. To view a copy of this licence, visit <http://creativecommons.org/licenses/by/4.0/>.

## REFERENCES

1. A. Morad and Y. Shash: *Int. Conf. Appl. Mech. Mech. Eng.*, 2014, vol. 16, pp. 1–22.
2. W. Jiang, P. Li, W.-X. Yao, S.-S. Rui, H.-J. Shi, and J. Huang: *Int. J. Fatigue*, 2021, vol. 147, 106191.
3. Smith, R., Lewi, G., Yates, D. Aircraft engineering and aerospace technology (2001).
4. R.C. Reed: *The Superalloys: Fundamentals and Applications*, Cambridge University Press, Cambridge, 2006. <https://doi.org/10.1017/CBO9780511541285>.
5. T.V. Sai, T. Vinod, and G. Sowmya: *Eng. Technol.*, 2017, vol. 3(2), pp. 463–68.
6. N. D'Souza: *Mater. Sci. Technol.*, 2009, vol. 25(2), pp. 170–78.
7. A.K. Gupta, B.K. Saxema, S.N. Tiwari, and S.L. Malhorta: *J. Mater. Sci.*, 1992, vol. 27, pp. 853–62.
8. G. Sigworth and C. Wang: *Metall. Trans. B*, 1993, vol. 24B, pp. 349–64.
9. K. Pang and H. Yuan: *Int. J. Fatigue*, 2020, vol. 136, 105575.
10. A. Cervellon, S. Hemery, P. Kurnsteiner, B. Gault, P. Kontis, and J. Cormier: *Acta Mater.*, 2020, vol. 188, pp. 131–44.
11. B. Bokstein, A. Epishin, T. Link, V. Esin, A. Rodin, and I. Svetlov: *Scripta Mater.*, 2007, vol. 57(9), pp. 801–04.
12. B. Rutttert, C. Meid, L. Mujica Roncery, I. Lopez-Galilea, M. Bartsch, and W. Theisen: *Scripta Mater.*, 2018, vol. 155, pp. 139–43.
13. K. Liu, J. Wang, B. Wang, P. Mao, Y. Yang, and Y. Zhou: *Mater. Charact.*, 2021, vol. 177, 111180.
14. J.-C. Gebelin and M.R. Jolly: *J. Mater. Process. Technol.*, 2003, vol. 135(2–3), pp. 291–300.
15. S. Roskosz: *Prac. Metallogr.*, 2013, vol. 50(8), pp. 527–47.
16. A. Torroba, O. Koeser, L. Calba, L. Maestro, E. Carreno-Morelli, M. Rahimian, S. Milenkovic, I. Sabirov, and J. Llorca: *Integr. Mater. Manuf. Innov.*, 2014, vol. 3, p. 25.
17. P.G.R. Deshpande: *Int. J. Innov. Eng. Res. Technol.*, 2019, vol. 3, pp. 1–4.
18. E. Abhilash and M. Joseph: *Indian Foundry J.*, 2009, vol. 55(10), pp. 28–37.
19. X. Yan, R. Nan Wang, Q. Xu, and B. Liu: *High Temp. Mater. Process. (London)*, 2017, vol. 36(4), pp. 327–37.
20. D. Szeliga, K. Kubiak, A. Burbelko, M. Motyka, and J. Sieniawski: *J. Mater. Eng. Perform.*, 2014, vol. 23(3), pp. 1088–95.
21. C. Ridgeway, C. Gu, K. Ripplinger, D. Detwiler, M. Ji, S. Sohgrati, and A. Luo: *Mater. Des.*, 2020, vol. 194, 108929.
22. L. Shark, C. Yu, J. Smith: *J. ROMA. 15th WCNDT*, 2000.
23. K. Heim, F. Bernier, R. Pelletier, and L.-P. Lefebvre: *Case Stud. Nondestruct. Test. Eval.*, 2016, vol. 6, pp. 45–52.
24. T. Kowaluk: *Pomiary Automatyka Robotyka*, 2012, vol. 16, pp. 82–86.
25. S. Tian, L. Bowen, B. Liu, F. Zeng, H. Xue, V. Erastova, H. Chris Greenwell, Z. Dong, R. Zhao, and J. Liu: *Fuel*, 2021, vol. 304, 121319.
26. L. Ouichou, F. Lavaud, G. Lesoult: *Proceedings of the Superalloys. Springer Nature 2021 LATEX template Identifying critical defect sizes using automated analysis*, 1980.
27. C. Pequet, M. Rappaz, and M. Gremaud: *Metall. Mater. Trans. A*, 2002, vol. 33A, pp. 2095–2106.
28. W. Walton: *Nature*, 1948, vol. 162(4113), pp. 329–30.

29. Y. Murakami: *Eng. Fract. Mech.*, 1985, vol. 22(1), pp. 101–14.
30. Y. Murakami and M. Endo: *Int. J. Fatigue*, 1994, vol. 16(3), pp. 163–82.
31. I. Ozturk: Automated evaluation of standard defect sizes for casting porosity. Master's thesis, Technische Universitat Munchen, 2021.
32. J. Yousefi: Ontario, Canada: University of Guelph, 2011.
33. <https://docs.opencv.org/3.4/d9/db0/tutorialhoughlines.html>. Accessed Aug 2021.
34. S. Lloyd: *IEEE Trans. Inf. Theory*, 1982, vol. 28(2), pp. 129–37.
35. I.T. Jolliffe and J. Cadima: *Philos. Trans. R. Soc. A*, 2016, vol. 374(2065), p. 20150202.
36. C. Krammer: Korrelation der flächenporosität mit der gröÙe des risskeims in der nickelbasis-superlegierung mar-m247. masterthesis, technical university of munich (tum), 2013.
37. Y. Murakami and S. Beretta: *Extremes*, 1999, vol. 2(2), pp. 123–47.
38. J.E. Spowart, H.E. Mullens, and B.T. Puchala: *JOM*, 2003, vol. 55(10), pp. 35–37.
39. T. Link, S. Zabler, A. Epishin, A. Haibel, M. Bansal, and X. Thibault: *Mater. Sci. Eng. A*, 2006, vol. 425(1), pp. 47–54.
40. S. Roskosz: *Arch. Metall. Mater.*, 2017, vol. 62, pp. 253–58.
41. M. Riedler, S. Michelic, and C. Bernhard: *IOP Conf. Ser.*, 2016, vol. 143(1), 012035.
42. L. Yang, L.H. Chai, L.Q. Zhang, and J. Lin: *Mater. Sci. Forum*, 2013, vol. 747, pp. 105–10.
43. J. Gumpinger, A. Brandao, E. Beevers, T. Rohr, T. Ghidini, S. Beretta, S. Romano: 2018.
44. D. Ma: *Front. Mech. Eng.* 2017, vol. 13.
45. D. O'Mahoney and D.J. Browne: *Exp. Thermal Fluid Sci.*, 2000, vol. 22(3), pp. 111–22.
46. Y. Zhou, B. Wang, S. Li, W. Li, K. Xu, J. Liang, F. Zhou, C. Wang, and J. Wang: *J. Alloy. Compd.*, 2022, vol. 897, 163169.

**Publisher's Note** Springer Nature remains neutral with regard to jurisdictional claims in published maps and institutional affiliations.